Supplementary Information (SI) for Energy & Environmental Science.

Supporting Information

Electron Push-Pull Engineering Enables Sustainable, Anti-Corrosive, and Nonflammable Phosphate Electrolytes for Long-Lifespan Lithium-Sulfur Batteries

Quanyan Man,[a, b, c] *Yongbiao Mu,*[a, b]* *Lin Yang,*[a, b] *Maokun Li,*[a, d] *Huicun Gu,*[a, b] *Xiaoqian Xu,*[a, b] *Zijian Qiu,*[a, b] *Chao Yang,*[d] *Meisheng Han,*[a, b] *Guangmin Zhou,*[c]* *Lin Zeng*[a, b]*

[a] Shenzhen Key Laboratory of Advanced Energy Storage, Department of Mechanical and Energy Engineering, Southern University of Science and Technology, Shenzhen 518055, P. R. China

[b] SUSTech Energy Institute for Carbon Neutrality, Southern University of Science and Technology, Shenzhen 518055, P. R. China

[c] Institute of Materials Research, Tsinghua Shenzhen International Graduate School, Tsinghua University, Shenzhen, 518055 P. R. China

[d] Key Laboratory of Natural and Biomedical Polymer Materials (Education Department of Guangxi Zhuang Autonomous Region), College of Materials Science and Engineering, Guilin University of Technology, Guilin 541004, P. R. China

* Corresponding authors: 12131093@mail.sustech.edu.cn (Yongbiao Mu); guangminzhou@sz.tsinghua.edu.cn (Guangmin Zhou); zengl3@sustech.edu.cn (Lin Zeng)

Experimental sections

Materials and electrolyte preparation

Electrolytes: 1,1,2,2-tetrafluoroethyl-2,2,3,3-tetrafluoropropyl ether (TTE), triethyl phosphate (TEP), p-methylanisole (pMA), phenetole (MA), anisole (AN), difluoroanisole (DFA), and p-fluoroanisole (pFA) were dried using 4 Å molecular sieves for 48 hours prior to use. The LH-pMA electrolyte was prepared by dissolving battery-grade lithium bis(trifluorosulfonyl)imide (LiFSI) in pMA and TEP, in which the the molar ratio of LiFSI : TEP : pMA is 1: 1.5 : 3. For comparison, LH-TTE, LH-MA, LH-AN, LH-DFA, and LH-pFA were prepared by replacing pMA with corresponding diluents in the same molar ratio. The H-TEP (LiFSI : TEP = 1 : 1.5) and L-TEP (1M LiFSI in TEP) were also formulated.

Electrodes: The sulfurized polyacrylonitrile (SPAN) cathode slurry was prepared by mixing SPAN powder, Super P conductive carbon, and polyvinylidene fluoride (PVDF) in a mass ratio of 8:1:1 using N-methylpyrrolidone (NMP) as the solvent. The slurry was uniformly coated onto aluminum foil and dried under vacuum at 80 °C for more than 12 hours. The areal loading of the cathode was approximately 3.5 mg cm^{-2}. Lithium iron phosphate (LFP) cathode with areal loading of 5.5 mg cm^{-2} was prepared by above method. The sulfur mass content in the purchased SPAN cathode is 47~50 wt%. Lithium metal foil was obtained from Canrd Co., Ltd.

Electrochemical testing

The oxidative stability of the electrolytes was evaluated by linear sweep voltammetry (LSV) using lithium–stainless steel (SS) cells. Ionic conductivity was measured via electrochemical impedance spectroscopy (EIS) with stainless steel symmetric cells. The exchange current density (j_0) was extracted from Tafel plots obtained from lithium–lithium symmetric cells. The activation energy (E_a) for the Li^+ desolvation process in each electrolyte was calculated from temperature-dependent EIS Nyquist plots (298.15–338.15 K) using the Arrhenius equation. The Coulombic efficiency (CE) of lithium plating/stripping was tested in lithium–copper half-cells using a Neware battery test system. The cycling performance of lithium–lithium symmetric cells was assessed by repeated lithium stripping/plating at a current density of 0.5 mA cm^{-2} with a fixed areal capacity of 1 mAh cm^{-2}. The dissolution of the solid electrolyte interphase (SEI) was examined in Li||Cu half-cells. The SEI was formed on the copper current collector within a voltage range of 0.05–2.0 V, and its loss was evaluated after storage periods of 50, 30, 15, and 5 hours. For lithium–LFP and Li–SPAN full cells, three initial formation cycles were carried out at 0.2C, followed by cycling at 0.5C (SPAN: 1C = 800 mAh g^{-1}; LFP: 1C = 170 mAh g^{-1}) within a voltage window of 1–3 V (SPAN) and 2.5-3.7 V (LFP). Rate capability was evaluated by varying the C-rate from 0.2C to 2C. The electrolyte-to-sulfur (E/S) ratio for Li||SPAN full cells is controlled at 7.1 μL • mg^{-1}.

Characterisation

This study systematically investigated the solvation structures of different electrolytes using Fourier-transform infrared spectroscopy (FTIR), Raman spectroscopy, and proton nuclear magnetic resonance (^{1}H NMR) spectroscopy. The liquid nuclear magnetic resonance (^{1}H NMR and ^{17}O NMR) spectrum was carried out on BRUKER AVANCE 400 spectrometer. The chloroform-d and H_2O were used as external reference for ^{1}H NMR and ^{17}O NMR, repectively. To evaluate lithium deposition morphology, a Li||Cu half-cell with a copper substrate was loaded with 5 mAh/cm^2 of lithium and examined via scanning electron microscopy (SEM). The morphology and composition of the solid electrolyte interphase (SEI) formed on the lithium metal surface were characterized using cryogenic transmission electron microscopy (cryo-TEM), X-ray photoelectron spectroscopy (XPS), and time-of-flight secondary ion mass spectrometry (TOF-SIMS). The surface morphology of the cycled SPAN cathode was analyzed by SEM. The composition of the cathode electrolyte interphase (CEI) was further determined through XPS analysis and TOF-SIMS.

Computational details

Molecular Dynamics Simulations: The initial models of all molecular structures were constructed using Materials Studio.[1] After construction, structural optimization was performed using the Forcite module in Materials Studio with the COMPASS III force field. Atomic charges were assigned based on the force field. During the calculations, electrostatic interactions were treated using the Ewald method, while van der Waals interactions were calculated using the atom-based method. During the calculation, a blended structure with a density of 0.3 g/cm^3 was constructed using the Construction module within the Amorphous Cell tool of Materials Studio. Simulations were performed using the NPT ensemble for structural optimization at a pressure of 101.3 kPa and a temperature of 25 °C. The optimization was conducted for 1 ns until the system density stabilized. The optimized structure was then selected for subsequent NVT ensemble simulations at 25 °C with a total duration of 2 ns. The first 1 ns was dedicated to structural equilibration to ensure the system reached a stable state, and the following 1 ns was used for data production. Finally, the mean square displacement (MSD) of lithium ions and solvent molecules, as well as the radial distribution functions (RDF) of various components, were obtained.

Quantum chemical calculations: Density functional theory (DFT) calculations were carried out using the DMol^3 module.[2] This method employs efficient three-dimensional numerical integration to evaluate matrix elements within the Ritz variational framework. A double numerical basis set with polarization functions (DND) was used for all atoms except hydrogen. Geometry optimization was performed using the generalized gradient approximation (GGA) with the Becke–Lee–Yang–Parr (BLYP) exchange-correlation functional. The convergence thresholds for energy, gradient, and displacement were set to 1×10^{-5} Ha, 0.004 Ha/Å, and 0.005 Å, respectively. The self-consistent field (SCF) convergence criterion was set to 1×10^{-5} Ha, and the direct inversion in the iterative subspace (DIIS) method was employed to accelerate SCF convergence.

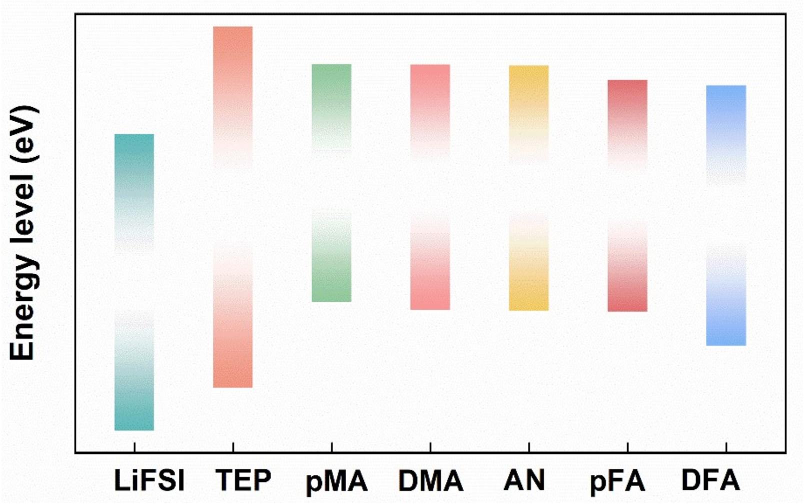

Figure S1 LUMO and HOMO energy levels of lithium salt and solvents.

Table S1 LUMO and HOMO energy levels of lithium salt and solvents.

Sample	LUMO (eV)	HOMO (eV)
LiFSI	-8.975	-1.882
TEP	-7.951	0.688
pMA	-5.888	-0.199
DMA	-6.077	-0.217
AN	-6.103	-0.237
pMA	-6.127	-0.588
DFA	-6.944	-0.717

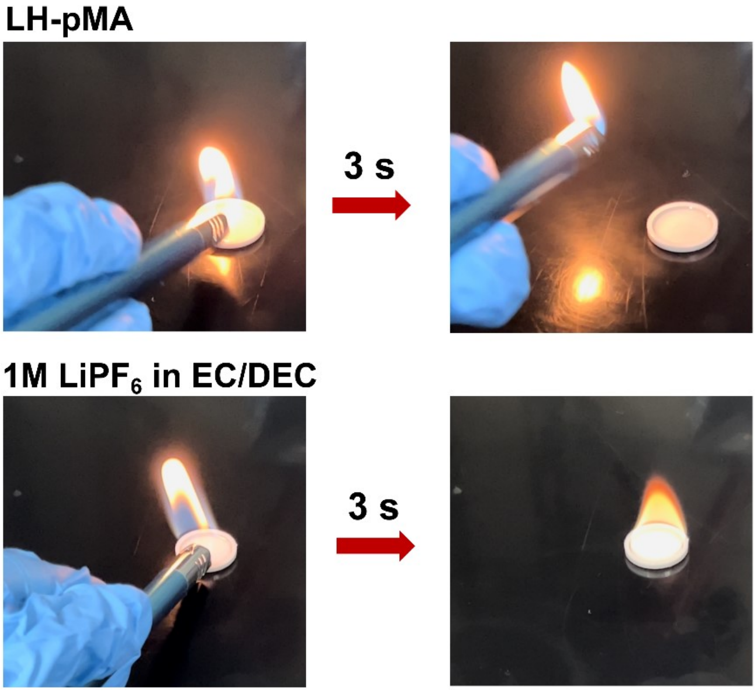

Figure S2 Flame-retardant test of LH-pMA and 1M $LiPF_6$ in EC/DEC.

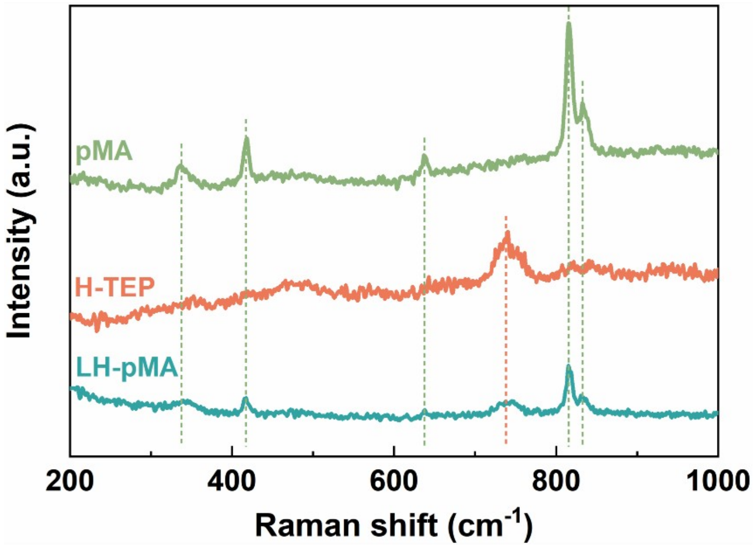

Figure S3 Raman spectra of pMA, H-TEP, and LH-pMA.

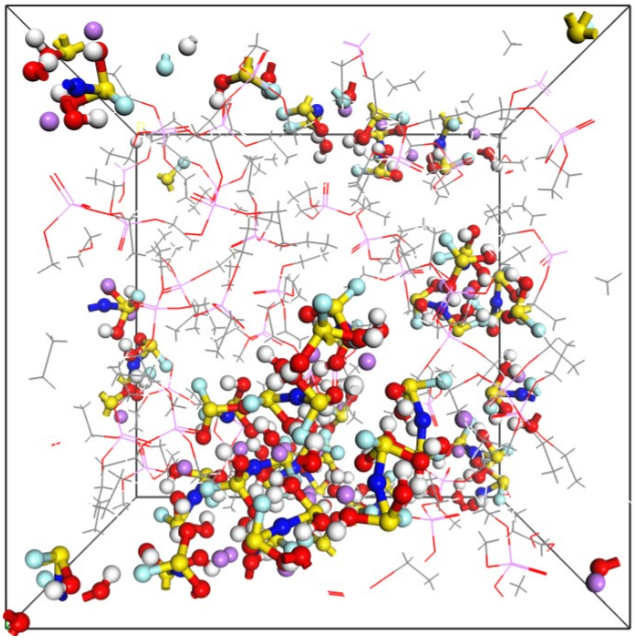

Figure S4 MD simulation snapshots of H-TEP.

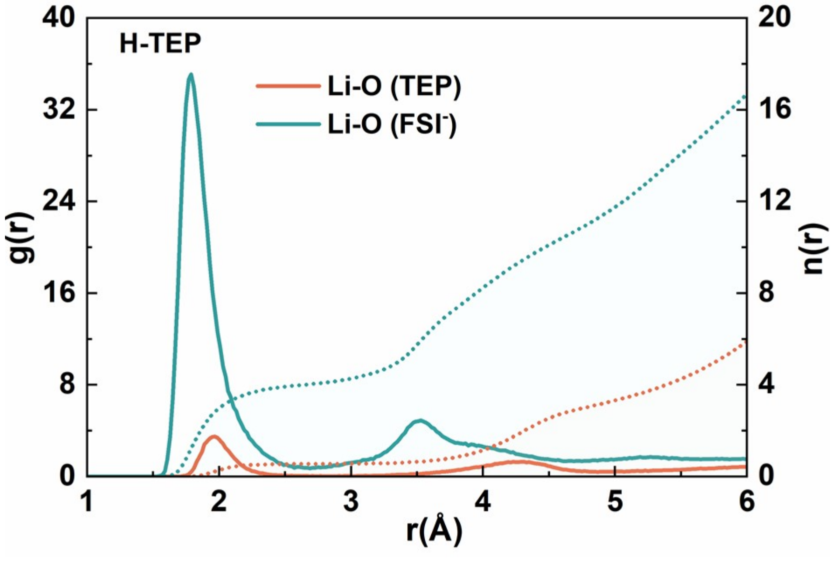

Figure S5 RDFs of H-TEP.

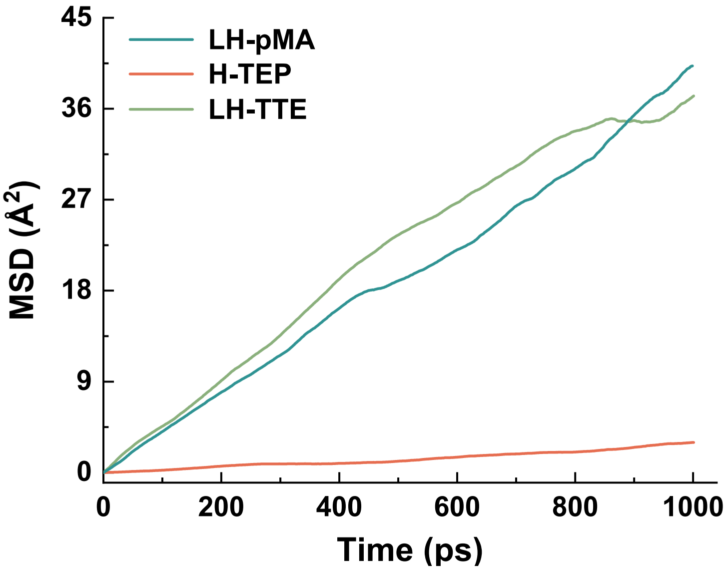

Figure S6 MSD calculations of FSI$^-$ diffusivity in different electrolytes.

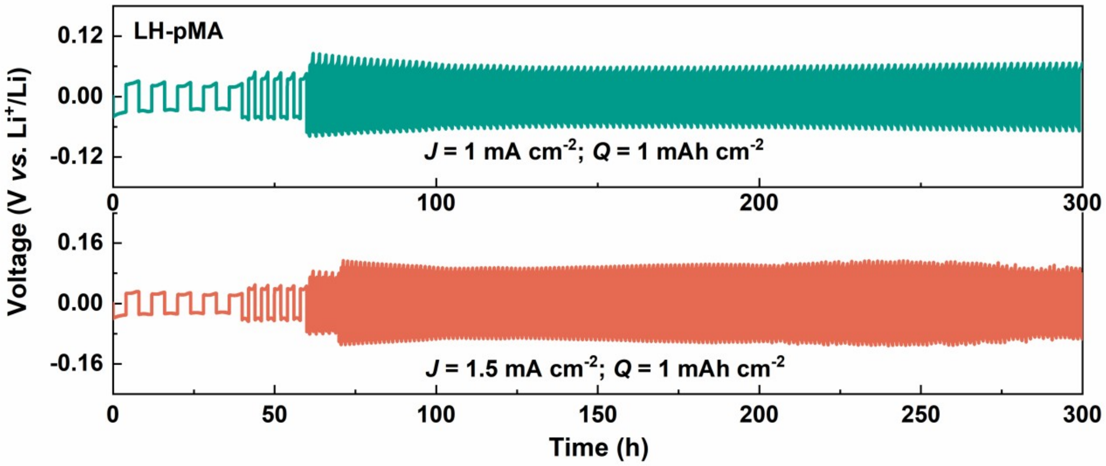

Figure S7 Cycling performance of Li||Li symmetric cells under 1 mA cm^{-2}/1.5 mA cm^{-2} and 1 mA h cm^{-2} using LH-pMA.

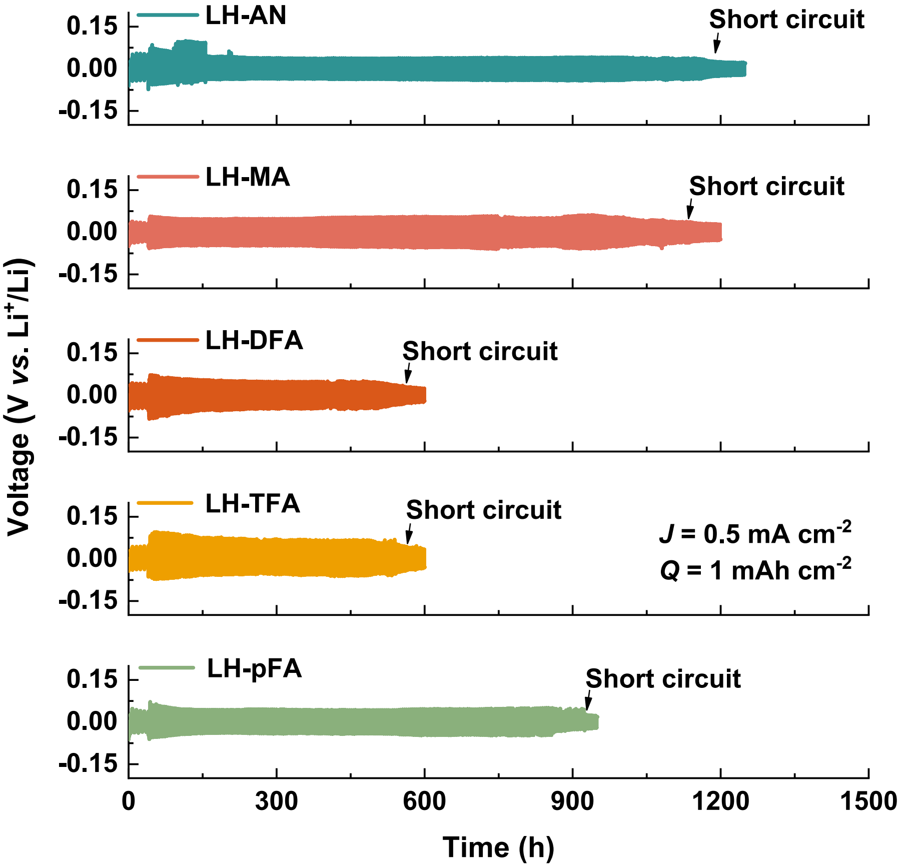

Figure S8 Cycling performance of Li||Li symmetric cells under 0.5 mA cm^{-2} and 1 mA h cm^{-2} using various electrolytes.

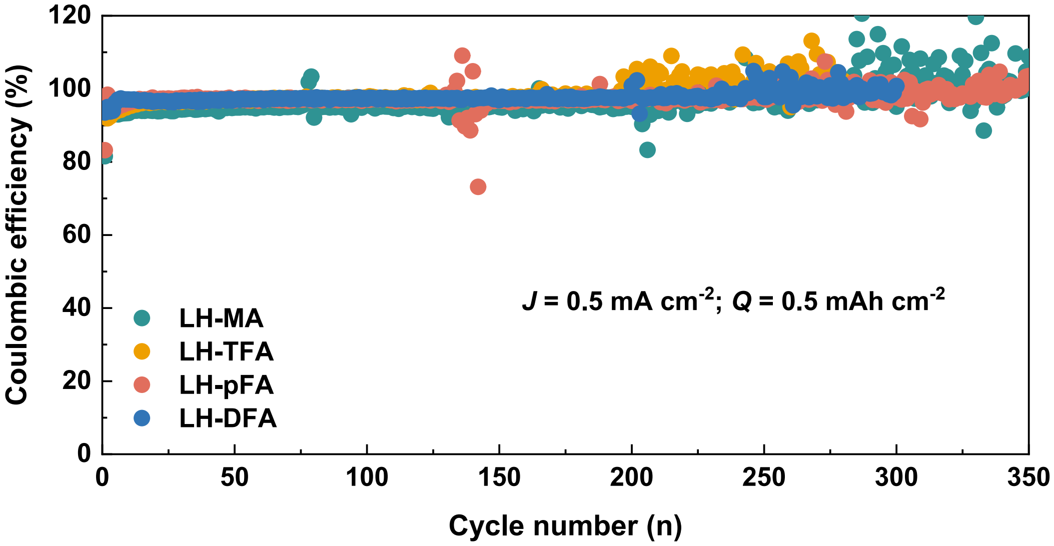

Figure S9 Li stripping/plating CEs in Li||Cu cells with various electrolytes under 0.5 mA cm^{-2} and 0.5 mA h cm^{-2}.

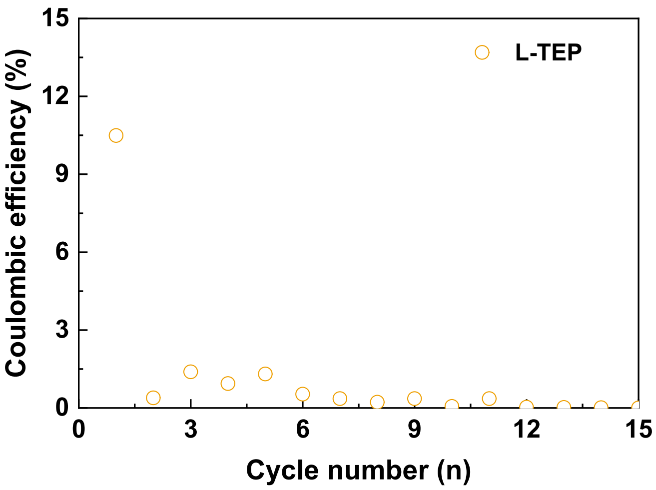

Figure S10 Li stripping/plating CEs in Li||Cu cells with L-TEP under 0.5 mA cm^{-2} and 0.5 mA h cm^{-2}.

Table S2 Comparison of LH-pMA in this work with previously reported TEP-based electrolytes.

Electrolyte	Current (mA cm^{-2})	Coulombic efficiency	Cycle number	Reference
LH-pMA	0.5	98.7%	650	This work
1.5 M LiTFSI in TEP with 0.47% LiNO3 and 4.53% DME	0.5	97%	400	ACS Nano, 2023, 17, 24227−24241
0.8 M LiFNFSI in FEBFP	0.5	99.3%	300	Nat. Commun., 2024, 15, 9856
1 M LiTFSI, 0.3 M LiDFOB, and 0.3 M $LiNO_3$ in TEP	0.25	93%	250	Energy Storage Mater., 2024, 71, 103603
2 M $LiNO_3$ in TEP and EC	0.5	96%	200	Energy Storage Mater., 2023, 59, 102782
1 M LiTFSI and 0.5 M $LiNO_3$ in TEP	0.5	94%	200	ACS Energy Lett., 2025, 10, 1700−1711

2.2 M LiFSI in TEP with FEC and LiBOB	0.25	99%	140	Nat. Energy, 2018, 3, 674-681
1.7 M LiFSI in TEP and DBE	0.5	99.4%	120	Adv. Mater., 2024, 36, 2406594
1.5 M LiNO3 in TEP and FEC	1	98.31%	120	Adv. Funct. Mater., 2023, 33, 2212605
1.5 M LiFSI in DCEP and TTE	0.5	98%	100	J. Am. Chem. Soc., 2024, 146, 28770−28782

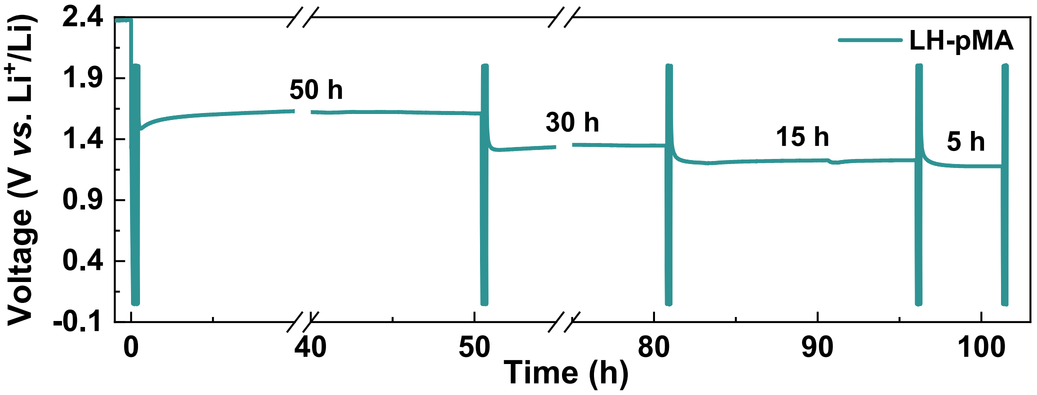

Figure S11 The voltage curves of Li||Cu cell with LH-pMA at different resting time.

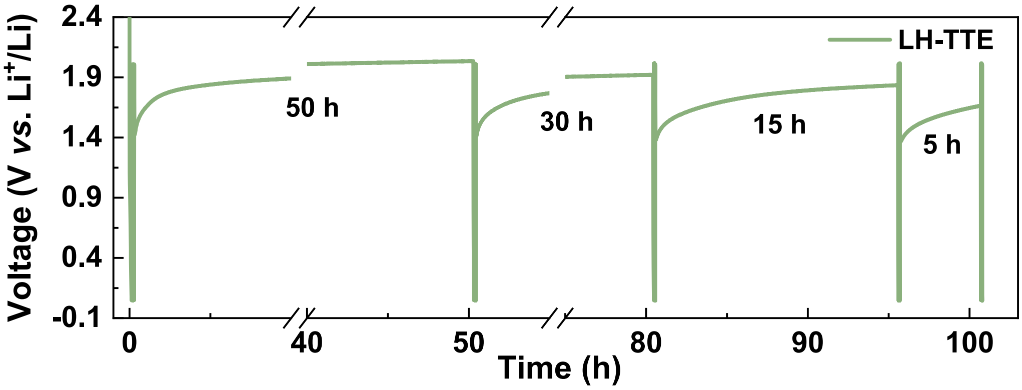

Figure S12 The voltage curves of Li||Cu cell with LH-TTE at different resting time.

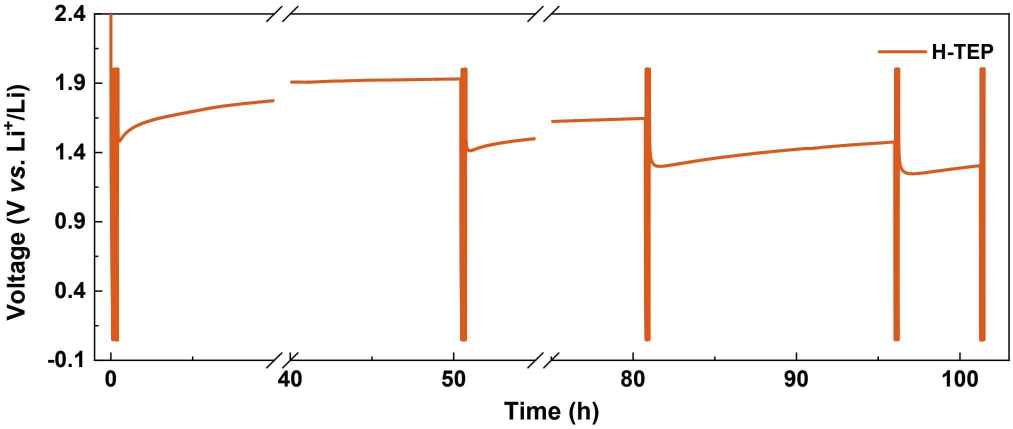

Figure S13 The voltage curves of Li||Cu cell with H-TEP at different resting time.

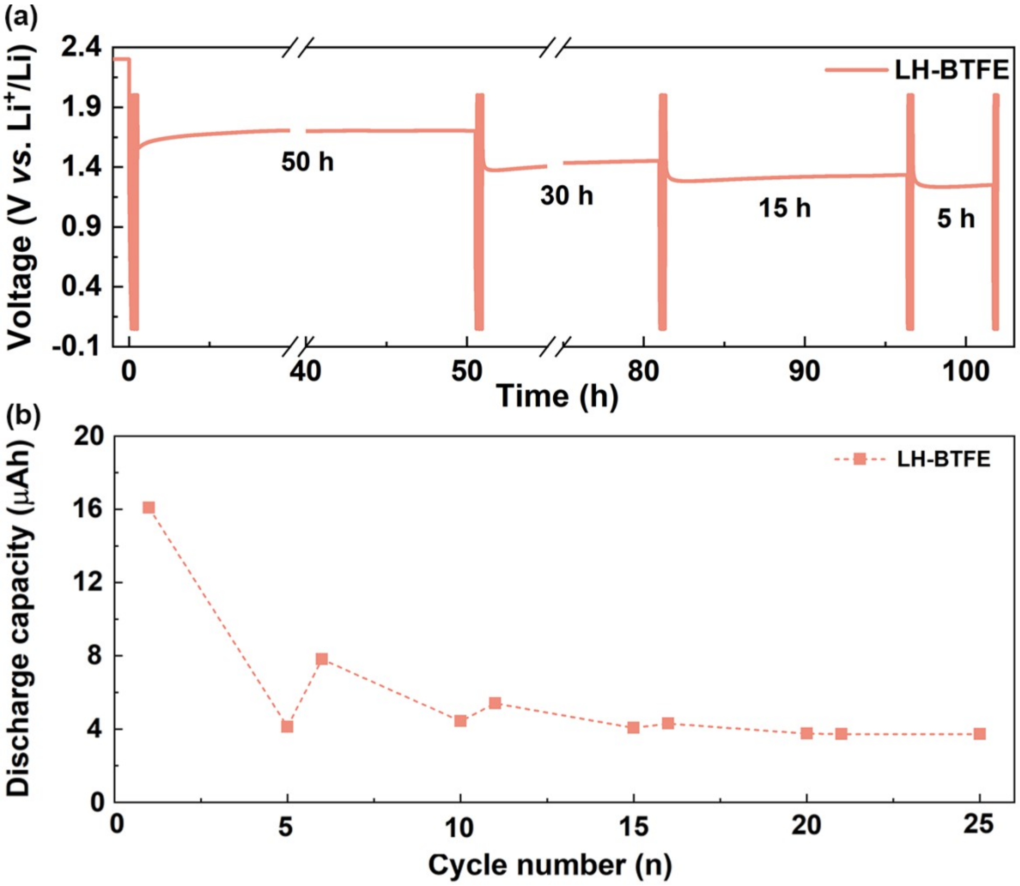

Figure S14 (a) The voltage curves of Li||Cu cell with LH-BTFE at different resting time. (b) Function of active lithium loss associated with SEI dissolution and relaxation time

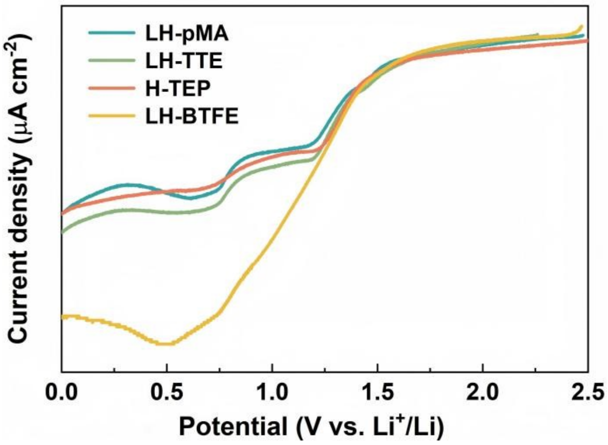

Figure S15 LSV reduction of Li||Cu cells at a scan rate of 0.01 mV s^{-1} from 2.5 V to 0 V.

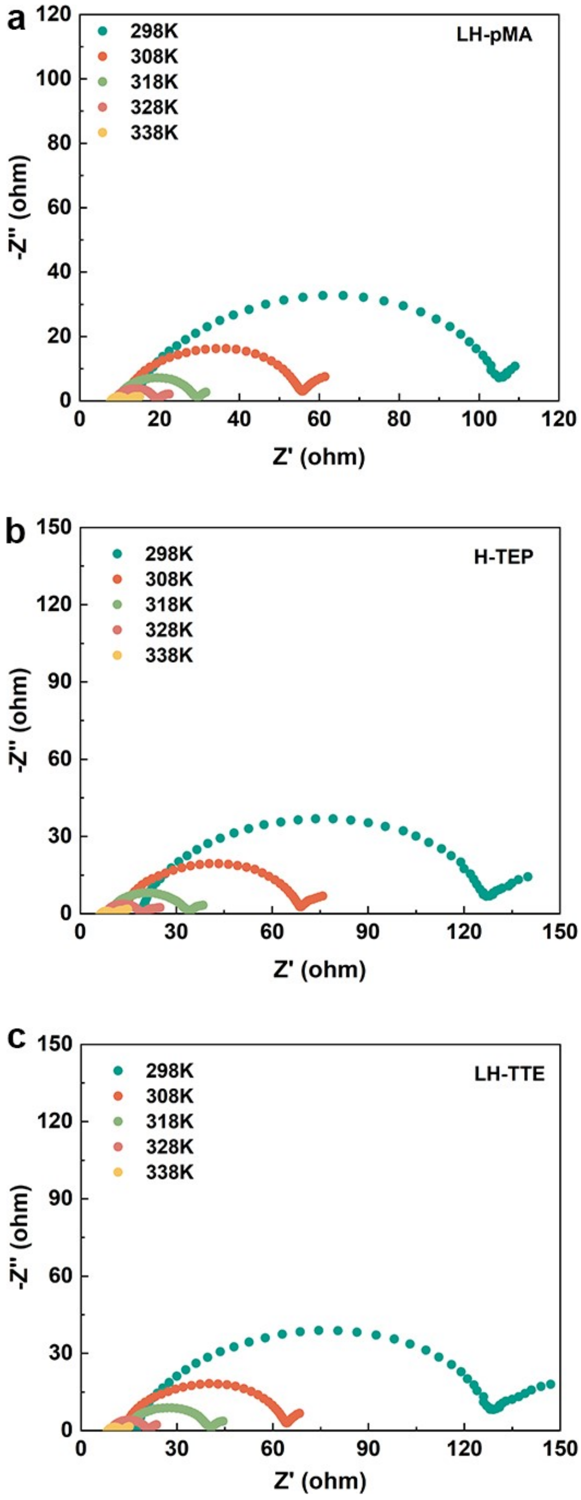

Figure S16 EIS profiles of (a) LH-pMA, (b) H-TEP, and (c) LH-TTE at different temperatures.

Table S3 The elements distribution of cycled Li anode in H-TEP electrolyte under different etching depth.

Elements	**N**	**O**	**F**	**S**	**C**
0s	7.67	34.69	14.33	15.16	28.16
30s	4.45	26.85	50.16	9.74	8.8
60s	3.24	30.03	53.88	7.22	5.63
90s	2.92	31.98	51.94	7.34	5.82
120s	2.16	33.34	50.9	7.77	5.82

Table S4 The elements distribution of cycled Li anode in LH-TTE electrolyte under different etching depth.

Elements	**N**	**O**	**F**	**S**	**C**
0s	9.07	38.03	21.74	17.47	13.69
30s	3.68	27.41	52.94	10.17	5.8
60s	2.9	29.56	53.39	9.16	4.98
90s	3.03	30.4	52.96	9	4.61
120s	2.04	31.29	52.56	8.9	5.21

Table S5 The elements distribution of cycled Li anode in LH-pMA electrolyte under different etching depth.

Elements	**N**	**O**	**F**	**S**	**C**
0s	8.26	39.06	19.96	9.81	22.91
30s	3.64	40.09	33.77	10.44	12.07
60s	3.21	40.96	36.74	9.66	9.44
90s	3.21	41.44	36.51	10.32	8.51
120s	2.35	39.26	35.06	9.83	13.49

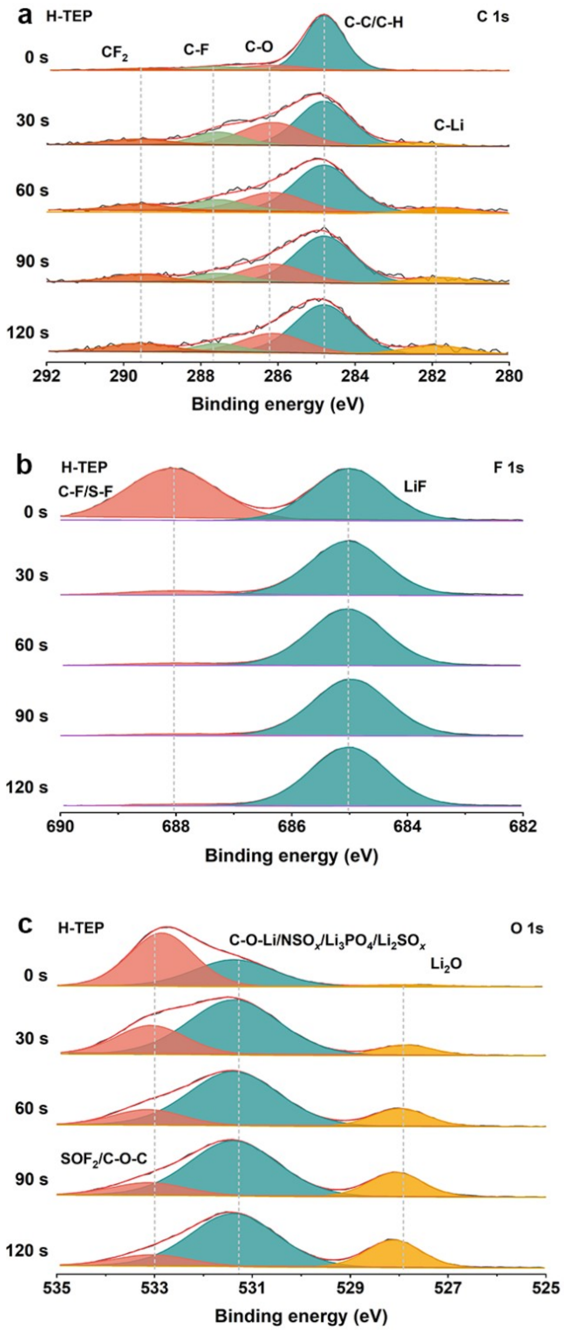

Figure S17 (a) C 1s, (b) F 1s, and (c) O 1s XPS analysis of lithium metal deposited in H-TEP electrolyte.

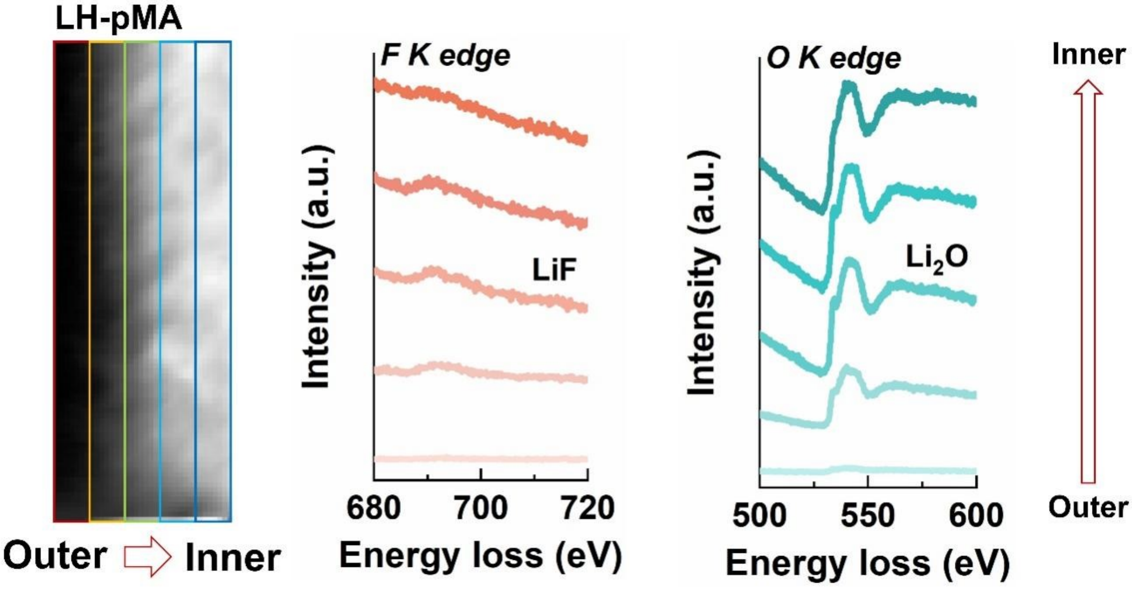

Figure S18 ADF-STEM image of SEI formed in LH-pMA and its corresponding EELS spectra of F K-edge and O K-edge.

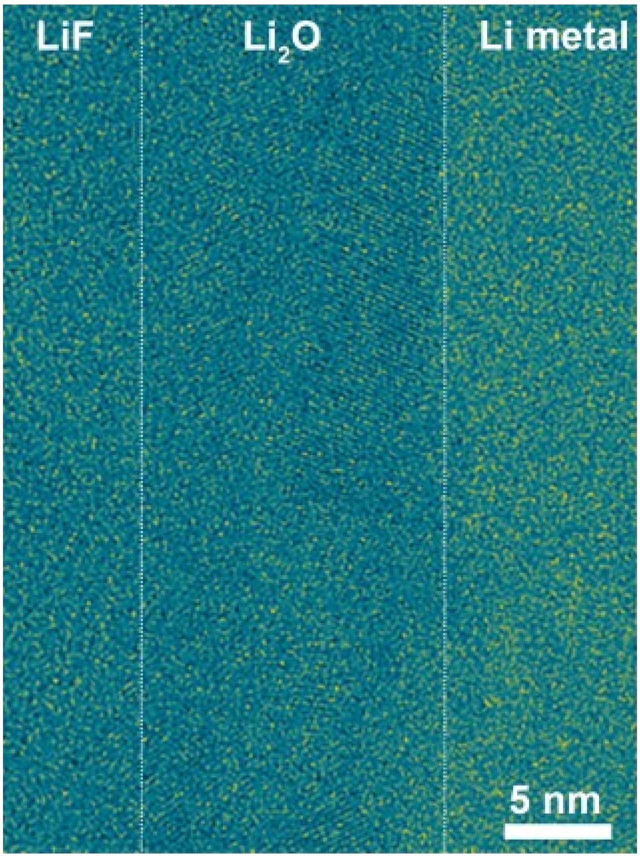

Figure S19 High-Resolution cryo-TEM image of SEI formed in LH-pMA.

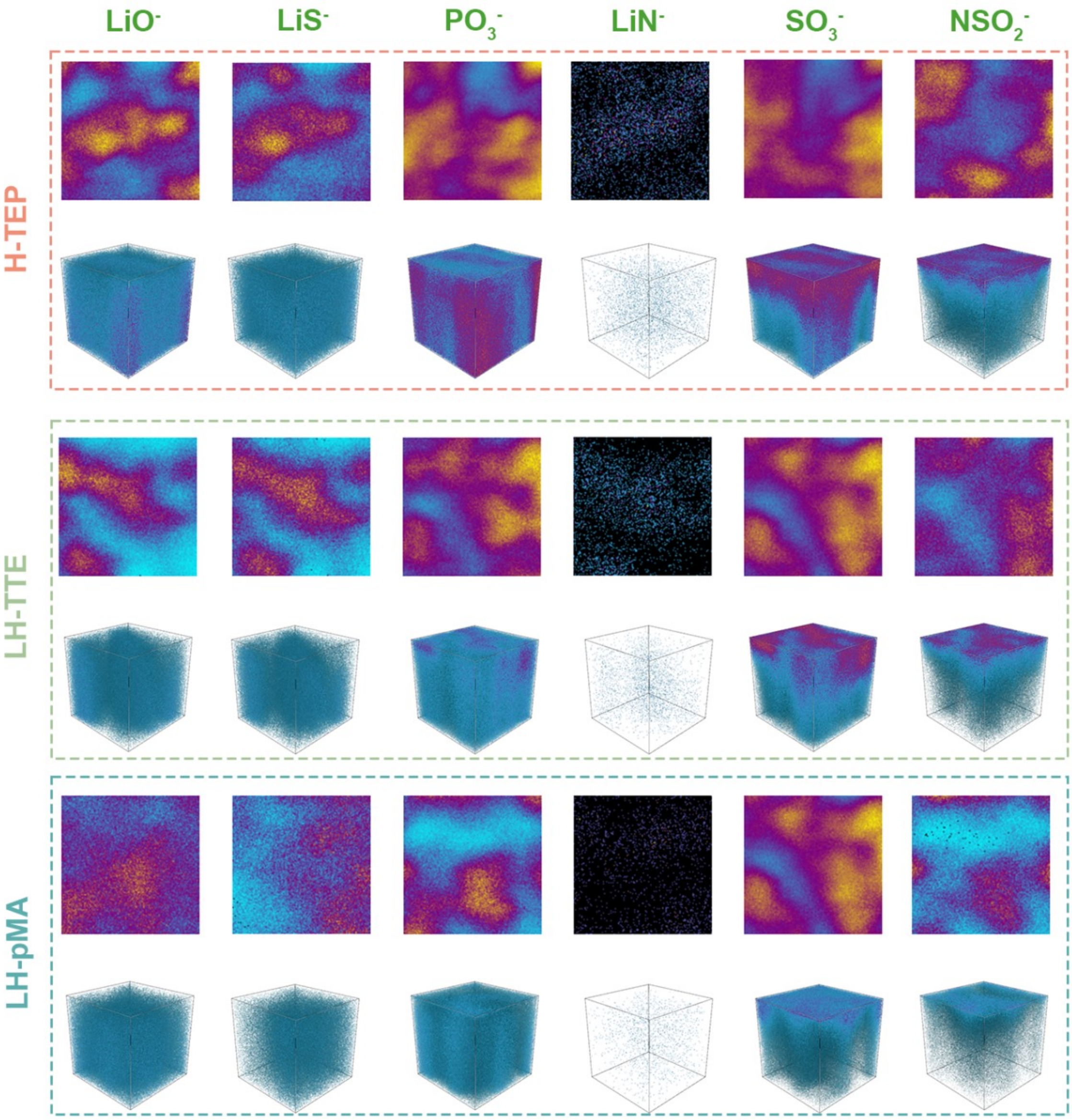

Figure S20 3D distribution of LiO$^-$, LiS$^-$, PO$_3^-$, LiN$^-$, SO$_3^-$, and NSO$_2^-$ species of lithium metal desposited in different electrolytes.

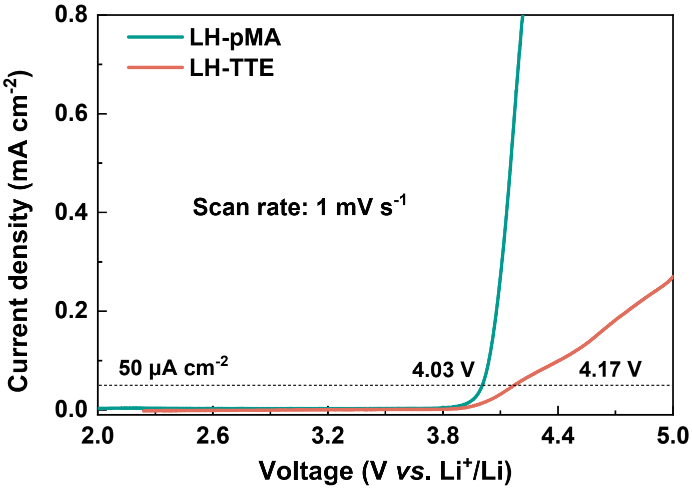

Figure S21 LSV profiles of LH-pMA and LH-TTE.

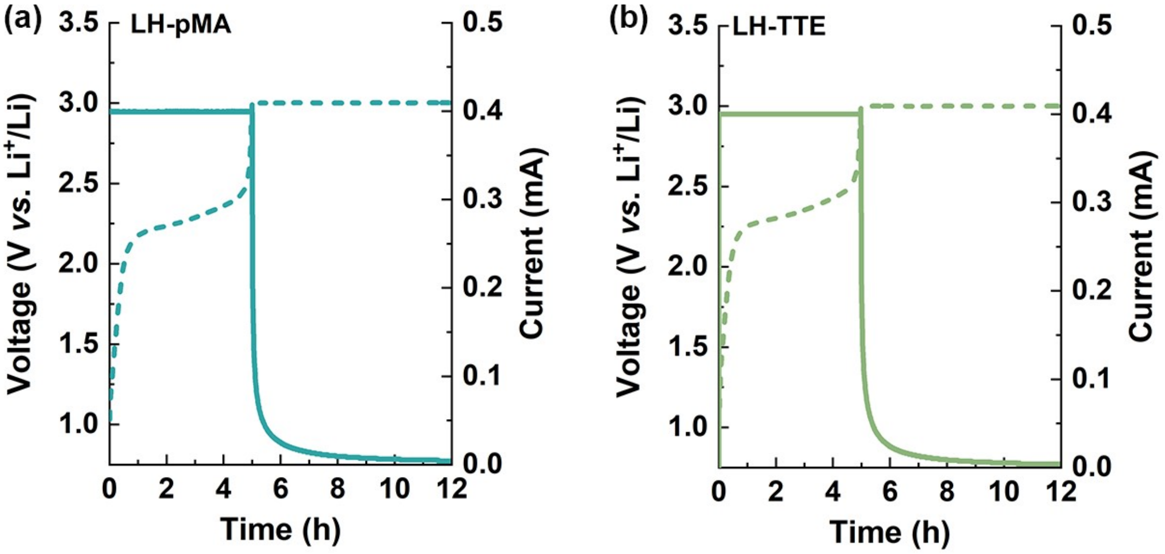

Figure S22 The voltage–time curves and current–time curves of Li||SPAN cells with (a) LH-pMA and (b) LH-TTE electrolytes.

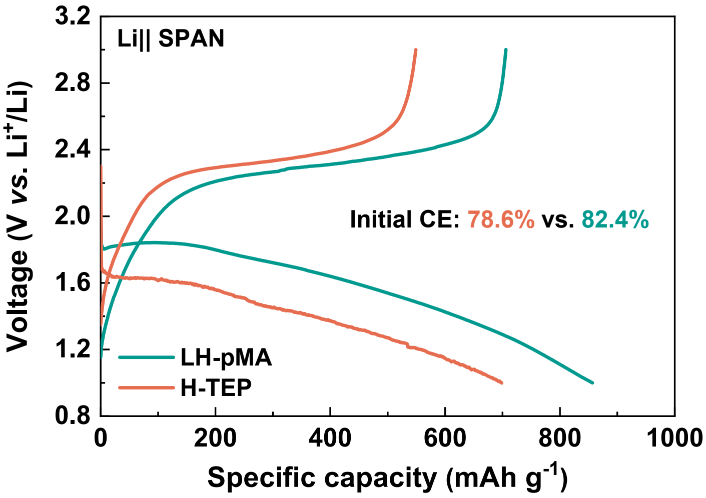

Figure S23 The initial charge-discharge profiles of Li||SPAN full cells with different electrolytes.

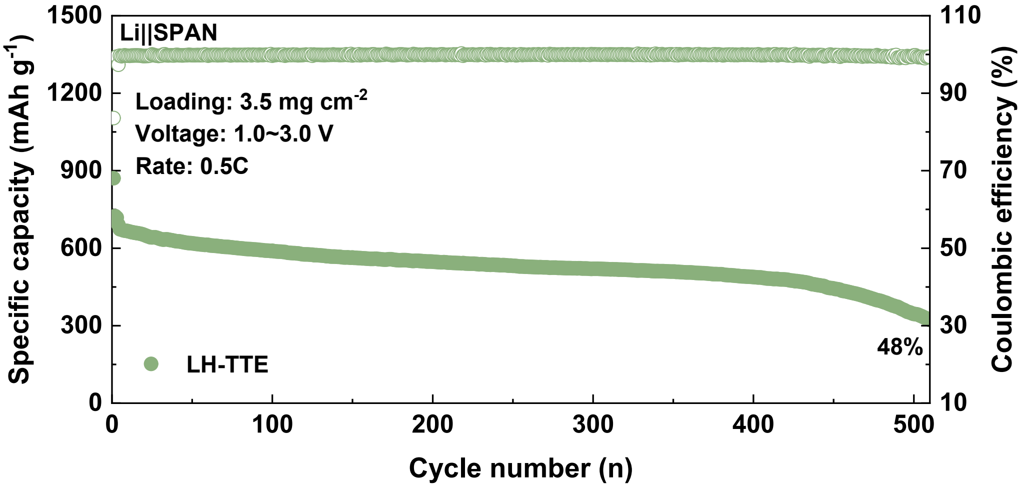

Figure S24 Cycling performance of Li||SPAN full cell with LH-TTE.

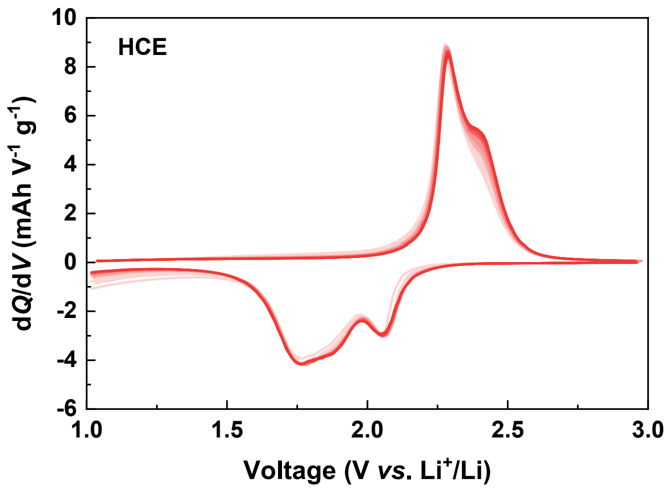

Figure S25 The dQ/dV profiles of Li||SPAN full cells cycled in H-TEP.

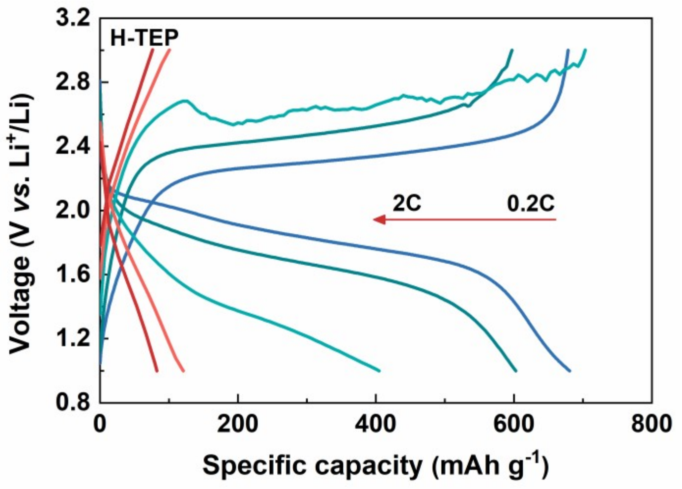

Figure S26 Discharge/charge profiles of Li||SPAN full cell at different rate.

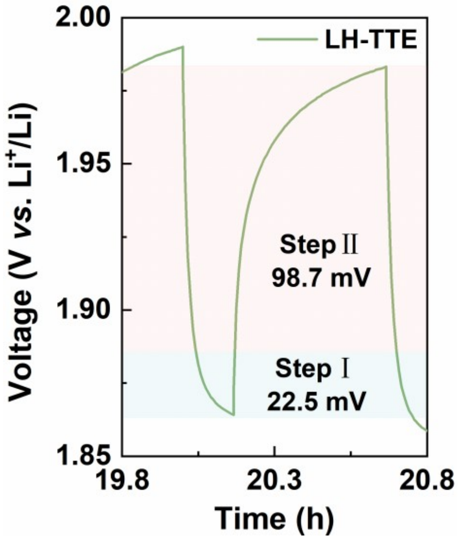

Figure S27 The enlarged GITT curve of Li||SPAN full cell in LH-TTE.

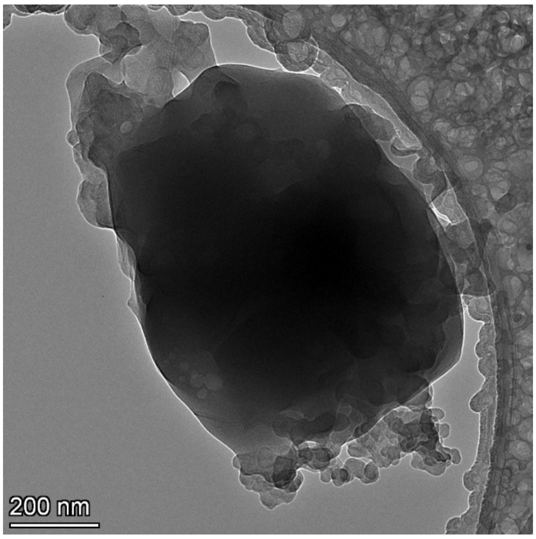

Figure S28 Cryo-TEM image of SPAN cycled in LH-pMA.

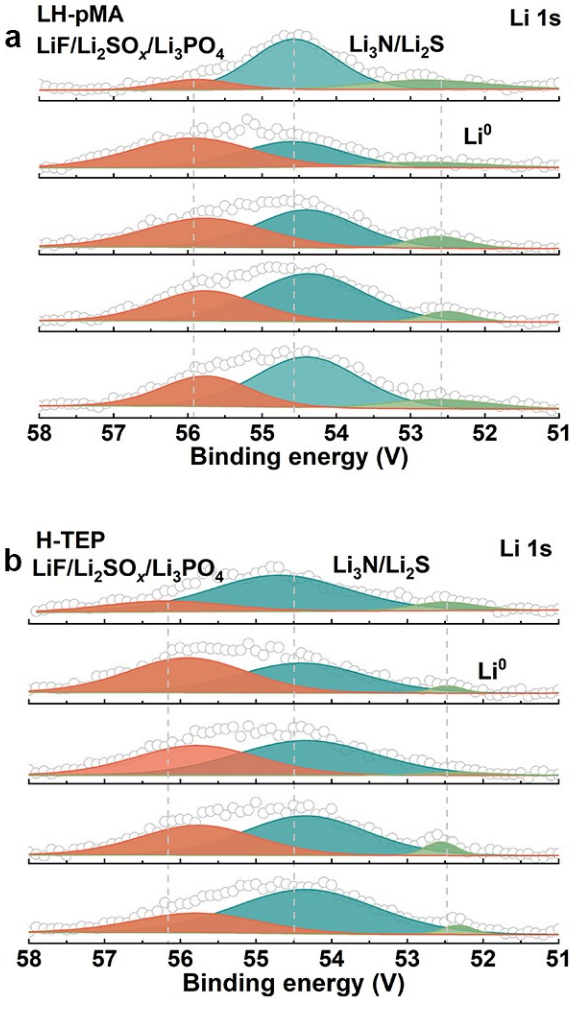

Figure S29 Li 1s XPS profiles of CEI in the (a) LH-pMA and (b) H-TEP.

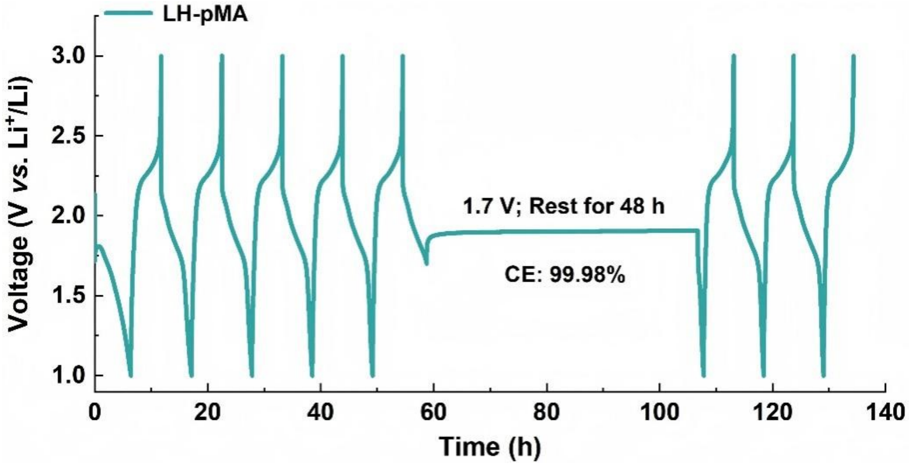

Figure S30 Self–discharge test of Li-SPAN cell at 1.7 V with LH-pMA.

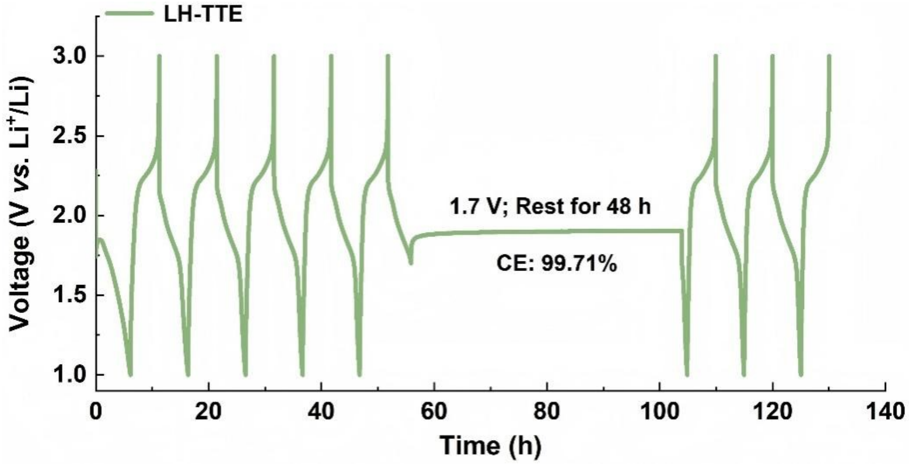

Figure S31 Self–discharge test of Li-SPAN cell at 1.7 V with LH-TTE.

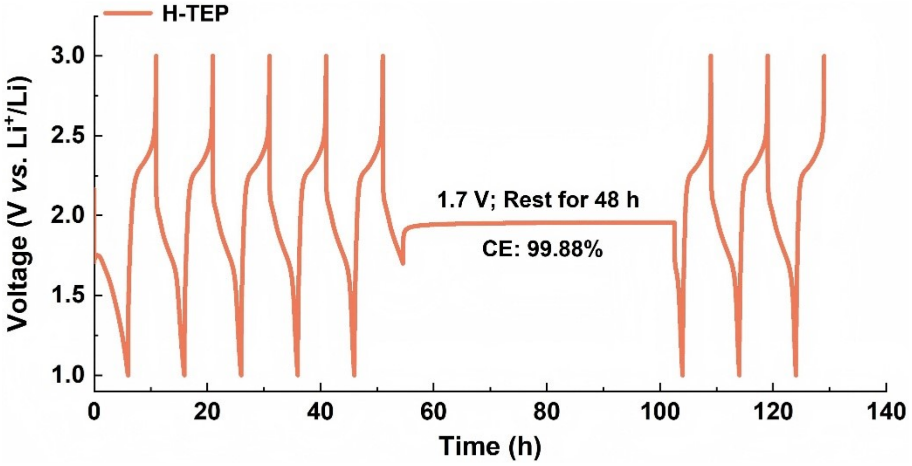

Figure S32 Self–discharge test of Li-SPAN cell at 1.7 V with H-TEP.

Reference

1. H. Sun, *J. Phys. Chem. B*, 1998, **102**, 7338-7364.
2. B. Delley, *Comput. Mater. Sci.*, 2000, **17**, 122-126.